

# THE ISOTHERMAL OUTFLOW IN THE MASSIVE STAR-FORMING REGION G240.31+0.07

JUNHAO LIU,<sup>1</sup> KEPING QIU,<sup>1,2</sup> FRIEDRICH WYROWSKI,<sup>3</sup> KARL MENTEN,<sup>3</sup> ROLF GÜSTEN,<sup>3</sup> YUE CAO,<sup>1</sup> AND YUWEI WANG<sup>1</sup>

<sup>1</sup>*School of Astronomy and Space Science, Nanjing University, 163 Xianlin Avenue, Nanjing 210023, P.R.China*

<sup>2</sup>*Key Laboratory of Modern Astronomy and Astrophysics (Nanjing University), Ministry of Education, Nanjing 210023, P.R.China*

<sup>3</sup>*Max-Planck-Institut für Radioastronomie, Auf dem Hügel 69, 53121 Bonn, Germany*

## ABSTRACT

We present Atacama Pathfinder Experiment (APEX) observations toward the massive star-forming region G240.31+0.07 in the CO J = 3-2, 6-5, and 7-6 lines. We detect a parsec-sized, bipolar, and high velocity outflow in all the lines, which allow us, in combination with the existing CO J = 2-1 data, to perform a multi-line analysis of physical conditions of the outflowing gas. The CO 7-6/6-5, 6-5/3-2, and 6-5/2-1 ratios are found to be nearly constant over a velocity range of  $\sim 5 - 25 \text{ km s}^{-1}$  for both blueshifted and redshifted lobes. We carry out rotation diagram and large velocity gradient (LVG) calculations of the four lines, and find that the outflow is approximately isothermal with a gas temperature of 50 K, and that the CO column density clearly decreases with the outflow velocity. If the CO abundance and the velocity gradient do not vary much, the decreasing CO column density indicates a decline in the outflow gas density with velocity. By comparing with theoretical models of outflow driving mechanisms, our observations and calculations suggest that the massive outflow in G240.31+0.07 is being driven by a wide-angle wind and further support a disk mediated accretion at play for the formation of the central high-mass star.

*Keywords:* ISM: individual objects (G240.31+0.07) - ISM: jets and outflows - stars: formation

## 1. INTRODUCTION

Bipolar molecular outflows, mostly observed in rotational transitions of CO, SiO and some other molecules, are a common phenomenon associated with young stellar objects (YSOs) of all masses (Zhang et al. 2001; Beuther et al. 2002a; Wu et al. 2004, 2005; Maud et al. 2015). It is believed that molecular outflows trace the accretion-powered ejections in sites of low-mass star formation, and they play an important role in the star formation process because of their significant impacts on the surrounding material and the parent cloud. Although molecular outflows have been extensively observed, their driving mechanism remains unknown. Molecular outflows from low-mass YSOs were thought to be produced by the interaction between wide-angle winds and the ambient gas (Shu et al. 1991; Lee et al. 2001), or by jet bow shocks (Raga & Cabrit 1993; Masson & Chernin 1993; Lee et al. 2001). Although the wind-driven model and the jet-driven model can both explain some observed outflow features, none of them are capable of pro-

ducing all of the observed features of different types of outflows (Lee et al. 2000, 2002). Two-component models with both a highly collimated jet and a wide-angle wind were then developed to establish a unified picture of the observed outflow features (Shu et al. 2000; Banerjee & Pudritz 2006; Pudritz et al. 2006; Shang et al. 2006; Pudritz et al. 2007; Machida et al. 2008).

Massive molecular outflows, which are associated with high-mass YSOs, are less understood than their low-mass counterparts. Due to the rarity and typically large distances, there are few studies toward outflows driven by massive YSOs. Although observations have shown that the morphology and kinematics of some massive outflows are very similar to what is observed for those driven by low-mass YSOs (Shepherd et al. 1998; Beuther et al. 2002b; Qiu et al. 2009; Ren et al. 2011), extremely collimated outflows and circumstellar disks have remained elusive for sources more massive than those equivalent to early B-type stars (Arce et al. 2007). And there is a lack of theoretical work on modeling outflows from high-mass YSOs. Many questions, e.g., how the outflows from massive YSOs are accelerated, how they differ from low-mass outflows, and how they affect the high-mass star-forming processes, are still unanswered.

Most previous studies of outflows have used low-J rotational transitions of CO (transitions up to  $J_u = 3$ , with upper-state energies  $E_u$  up to 30 K), which are readily excited at low temperatures and can be easily observed by ground-based facilities, to characterize the morphology and kinematics of the relatively cold and extended molecular gas. Due to the Earth's atmosphere, mid-J CO lines (referring to CO 6-5 and CO 7-6 throughout this paper, with  $E_u$  up to 150 K), which are less affected by the ambient gas, are not commonly observed. In several studies, mid-J CO transitions have been reported to trace the warm gas ( $T > 50$  K) in outflows of low-mass and intermediate-mass YSOs (van Kempen et al. 2009a,b; Yıldız et al. 2012; van Kempen et al. 2016). By comparing multi-line CO observations (both low-J and mid-J) with the results of radiative transfer models, the physical properties (temperature, gas density and CO column density) of the outflowing gas could be better constrained (Lefloch et al. 2015).

This paper is a follow-up study of the G240.31+0.07 (hereafter G240) outflow (Qiu et al. 2009). We report the 12-m submillimeter Atacama Pathfinder Experiment Telescope<sup>1</sup> (APEX) observations of G240, an active high-mass star-forming region associated with IRAS 07427-2400 and located at a distance of 5.4 kpc (Choi et al. 2014; Sakai et al. 2015). It harbors an ultracompact HII region and is associated with OH and H<sub>2</sub>O masers (Hughes & MacLeod 1993; Caswell 1997; MacLeod et al. 1998; Migenes et al. 1999; Caswell 2003). Its far-infrared luminosity of  $10^{4.7} L_\odot$  is consistent with a spectral type O8.5 zero-age main-sequence star (MacLeod et al. 1998). Kumar et al. (2003) mapped the CO 3-2 emission with a 20'' beam. From C<sup>18</sup>O 2-1 observations, Kumar et al. (2003) found the cloud velocity ( $v_{\text{cloud}}$ ) with respect to the local standard of rest to be  $\sim 67.5$  km s<sup>-1</sup>. Qiu et al. (2009) presented a detailed high-resolution study of CO 2-1 and <sup>13</sup>CO 2-1 emissions and detected a bipolar, wide-angle, quasi-parabolic molecular outflow. Li et al. (2013) theoretically interpreted the G240 outflow as a result from interaction between a wide-angle wind and the ambient gas in the form of turbulent entrainment. Recently, Qiu et al. (2014) reported the detection of an hourglass magnetic field aligned within 20° of the outflow axis.

In this paper, we present a CO multi-transition (2-1, 3-2, 6-5, 7-6) study toward the G240 outflow. With rotation diagram (RD) and large velocity gradient (LVG)

calculations, we estimate the physical parameters of the outflow as functions of gas velocity. We then discuss the results of the analysis.

## 2. OBSERVATIONS

The observations were performed with the 12 m APEX telescope. The APEX CO (6-5) and CO (7-6) observations were performed in 2010 July with the Carbon Heterodyne Array of the MPIfR (CHAMP+) (Kasemann et al. 2006). The APEX CO (3-2) observations were made in 2011 October using the First Light APEX Submillimeter Heterodyne (FLASH) receiver (Heyminck et al. 2006).

Pointings were checked by comparing these lines with the CO 2-1 data adopted from Qiu et al. (2009), and were found to be within  $\sim 7''$  for CO 3-2 and within  $\sim 4''$  for CO 6-5 and 7-6. The system temperatures were found to be ? at ? GHz. The ? spectrometer was used as the backend with a resolution of ? kHz (? km s<sup>-1</sup>). The data were smoothed to 2 km s<sup>-1</sup>, then the rms noises in the spectra in the central part of the map are of the order 0.03-0.05 K at 345 GHz, 0.15-0.25 K at 691 GHz and 0.40 - 0.60 K at 809 GHz at the central region of the maps. Noises are higher at the edge of the maps. Beam efficiencies, determined by observations of planets, were 0.65, 0.41 and 0.40 at 345 GHz, 691 GHz and 809 GHz, respectively. The APEX beam sizes are  $\sim 19''$  at 345 GHz,  $\sim 9''$  at 691 GHz and  $\sim 8''$  at 809 GHz. Calibration uncertainties were assumed to be 15 %, 20% and 30% at 345 GHz, 691 GHz and 809 GHz, relatively. These data were complemented with the previously observed combined data from the Submillimeter Array<sup>2</sup> (SMA) and the Caltech Submillimeter Observatory<sup>3</sup> (CSO) 10.4 m telescope in CO 2-1 (Qiu et al. 2009). The CO 2-1 data has a calibration uncertainty of 10 %, with the rms estimated to be 0.06-0.10 K in 2 km s<sup>-1</sup> channels. Table 1 shows a summary of the line informations.

## 3. RESULTS

### 3.1. CO emission maps

The CO 3-2, 6-5, and 7-6 emissions are detected (with obvious outflow signatures and with peak intensities  $> 2 \sigma_{\text{rms}}$ ) in velocity ranges from 42 to 94 km s<sup>-1</sup>, 44 to 92 km s<sup>-1</sup>, and 46 to 90 km s<sup>-1</sup>, respectively. Fig-

<sup>1</sup> The Atacama Pathfinder Experiment Telescope is a collaboration between the Max-Planck-Institut für Radioastronomie, the European Southern Observatory, and the Onsala Space Observatory.

<sup>2</sup> The Submillimeter Array is a joint project between the Smithsonian Astrophysical Observatory and the Academia Sinica Institute of Astronomy and the Astrophysics and is funded by the Smithsonian Institution and the Academia Sinica.

<sup>3</sup> The Caltech Submillimeter Observatory was supported by the NSF grant AST-0229008 and was decommissioned in 2015.

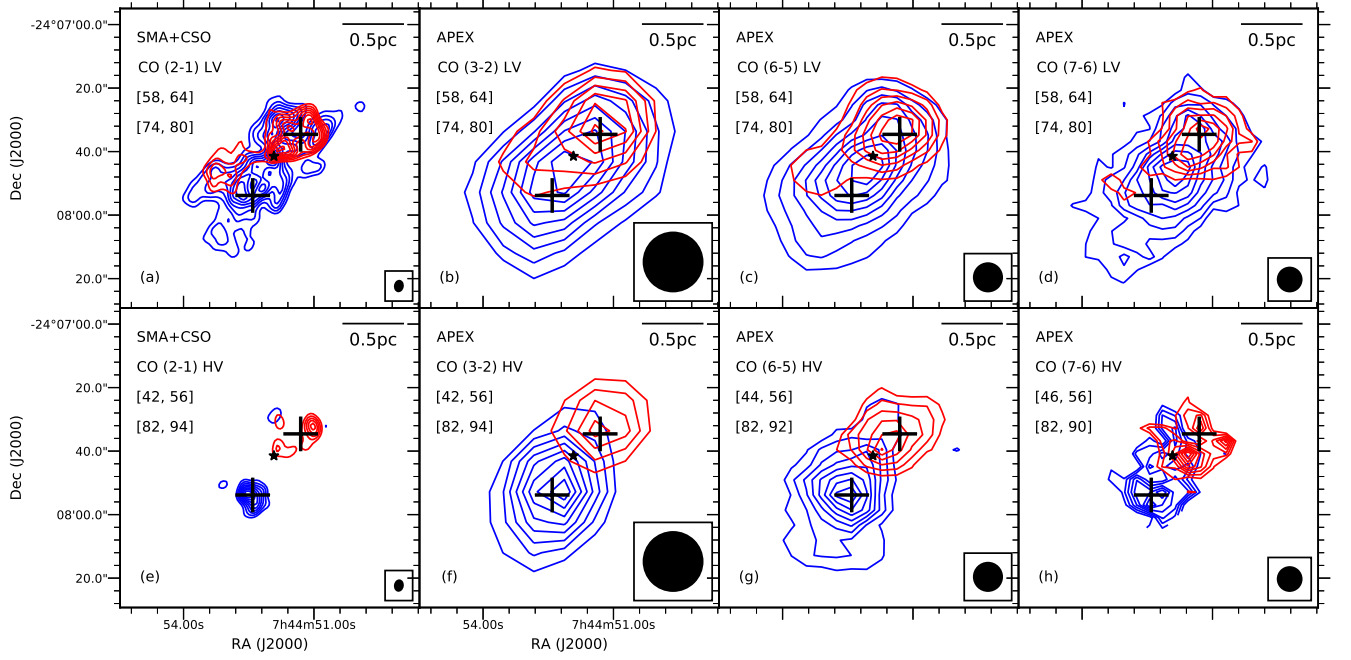


**Figure 1.** (a)-(d) Low-velocity CO  $J = 2-1, 3-2, 6-5, 7-6$  emissions, integrated from 58 to 64 km s<sup>-1</sup> for the blueshifted lobe (blue) and from 74 to 80 km s<sup>-1</sup> for the redshifted lobe (red); (e)-(f) High-velocity CO  $J = 2-1, 3-2$  emissions, integrated from 42 to 56 km s<sup>-1</sup> for the blueshifted lobe (blue) and from 82 to 94 km s<sup>-1</sup> for the redshifted lobe (red); (g) High-velocity CO  $J = 6-5$  emission, integrated from 44 to 56 km s<sup>-1</sup> for the blueshifted lobe (blue) and from 82 to 92 km s<sup>-1</sup> for the redshifted lobe (red) (h) High-velocity CO  $J = 7-6$  emission, integrated from 46 to 56 km s<sup>-1</sup> for the blueshifted lobe (blue) and from 82 to 90 km s<sup>-1</sup> for the redshifted lobe (red). For (a)-(g), the contour levels start from 20% and continue at steps of 10% of the peak emission. For (h), the contour levels start from 30% and continue at steps of 10% of the peak emission. Edge channels are masked out because of high noise levels. The black star marks the position of a H<sub>2</sub>O maser spot which is associated with IRAS 07427-2400 (Sakai et al. 2015). The beam of each observational dataset is shown in the lower right corner of each panel.

**Table 1.** Line informations

Line	Frequency	Beam size	$\sigma_{cal}$ <sup>a</sup>	$\sigma_{rms}$ <sup>b</sup>	$\eta_s$ <sup>c</sup>
	GHz	"	%	K	
CO 2-1	230.5380	$3.93 \times 3.10^d$	10	0.08	—
CO 3-2	345.7960	19.16	15	0.04	0.65
CO 6-5	691.4731	9.49	20	0.20	0.41
CO 7-6	806.6518	8.12	30	0.50	0.40

<sup>a</sup>Calibration error.

<sup>b</sup>Average rms in 2 km s<sup>-1</sup> channels.

<sup>c</sup>Beam efficiency.

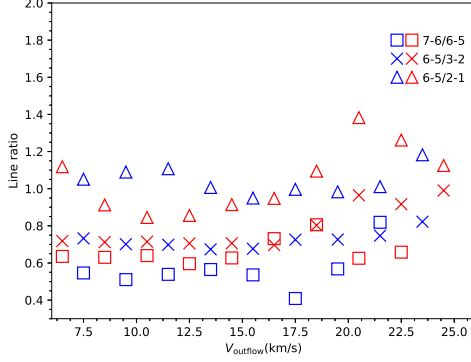
<sup>d</sup>Major axis  $\times$  minor axis.

Figure 1 shows the integrated low-velocity (LV) and high-velocity (HV) emissions of the four lines. The velocity ranges chosen to highlight the LV and HV components

of the outflowing gas follow those in Qiu et al. (2009), except that the channels with no detections were excluded for the HV component. The morphologies of the bipolar outflow seen in the CO 3-2, 6-5, and 7-6 lines are very similar. Due to the coarser angular resolutions, the wide-angle structure seen in the higher resolution CO 2-1 image is not seen in the CO 3-2, 6-5, 7-6 maps.

### 3.2. Physical conditions of the outflow

The physical condition of the outflow can be constrained by comparing the observed line intensities with the results of statistical-equilibrium calculations. To study the four lines at the same spatial resolution, the CO 2-1, 6-5, and 7-6 maps were reconstructed with the same beam of the CO 3-2 map. The rms noise levels are  $\sim 0.004$  K,  $\sim 0.04$  K and  $\sim 0.1$  K for the convolved CO 2-1, 6-5 and 7-6 data, respectively. For both lobes of the outflow, the CO line intensities were measured at approximately the peak positions of the HV components of the convolved CO maps (marked as two crosses in every panel of Figure 1), and were then used in the following



**Figure 2.** Ratios of the main-beam brightness temperatures of different CO lines at different velocities. Blue symbols denote the measurements from the blueshifted lobe, and red symbols the redshifted lobe. The  $V_{\text{outflow}}$  shown here is related to the cloud velocity  $v_{\text{cloud}}$  by the relation:  $V_{\text{outflow}} = |v_{\text{outflow}} - v_{\text{cloud}}|$ , where  $v_{\text{outflow}}$  is the outflow velocity with respect to the local standard of rest.

analysis. Figure 2 shows the ratios of the main-beam brightness temperatures ( $T_{\text{mb}}$ ) of different CO lines as functions of velocity. The CO 7-6/6-5, 6-5/3-2, and 6-5/2-1 ratios are almost constant over a velocity range of  $\sim 5 - 25$   $\text{km s}^{-1}$  with respect to the cloud velocity. In the analysis, we only used channels of  $\leq 60$   $\text{km s}^{-1}$  and  $\geq 74$   $\text{km s}^{-1}$  to avoid contaminations from the ambient gas, and we excluded channels of  $< 46$   $\text{km s}^{-1}$  or  $> 90$   $\text{km s}^{-1}$  because of their low signal-to-noise ratios. Since we didn't correct the observed line intensities for unknown beam filling factors, the derived CO column density, temperature, and gas density should be considered as beam-averaged values. In the calculation, errors on line intensities took into account both the uncertainties of the flux calibration uncertainty and the rms noise.

We first performed a simple rotation diagram (RD) analysis (Goldsmith & Langer 1999) to estimate the excitation condition of the outflowing gas under the assumption of local thermal equilibrium (LTE). Considering that the  $^{13}\text{CO}$  2-1 emission was only marginally detected at 60  $\text{km s}^{-1}$  and 78  $\text{km s}^{-1}$  (Qiu et al. 2009), we assumed the four  $^{12}\text{CO}$  lines to be optically thin at our considered velocities. The population of each energy level is given by

$$N_{\text{up}} = \frac{N_{\text{CO}}}{Z} g_{\text{up}} e^{-E_{\text{up}}/kT_{\text{kin}}}, \quad (1)$$

where  $N_{\text{up}}$  is the column density in the upper state,  $g_{\text{up}}$  the statistical weight of the upper state,  $E_{\text{up}}$  the upper energy level,  $k$  the Boltzmann constant, and  $Z$  is the partition function. The rotation diagram for CO at 84  $\text{km s}^{-1}$  is shown in Figure 3 as an example. An LTE model at 48.5 K could account for the measurements

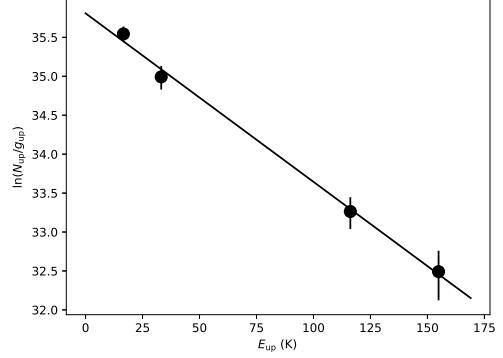


**Figure 3.** A rotation diagram for CO at 84  $\text{km s}^{-1}$ . The fitted line shows the Boltzmann distribution of the rotational populations. The line represents a rotational temperature of 48.5 K and a total column density of  $2.0 \times 10^{15} \text{ cm}^{-2}$ . The black solid circles show the data with error bars.

from the four lines. Other velocity channels show similar rotation diagrams.

To better constrain the gas temperature ( $T$ ), the density ( $n$ ), and the CO column density ( $N$ ) without assuming LTE and optical thin emission, we then performed radiative transfer calculations of the four lines using the RADEX code, which adopts the LVG approximation (van der Tak et al. 2007). We built a large grid of LVG models by varying the three parameters ( $n$ ,  $T$  and  $N$ ), and obtained the best fitting results by  $\chi^2$  minimization in comparing the observation with the models. With four lines observed and three parameters to constrain, our fitting had one degree of freedom. In Figure 4, the fitting results at 84  $\text{km s}^{-1}$  are shown. Figure 4(a) and Figure 4(b) show that the gas temperature is well constrained to *sim* 50 K. In Figures 4(b) and 4(c), the CO column density is stringently constrained to  $2.2 \times 10^{15} \text{ cm}^{-2}$ . The  $\chi^2$  distribution in Figure 4(a) and 4(c) indicate that in the best LVG models, the gas density is high enough to thermalize the emissions, and thus only lower limits of the gas density could be derived from the  $\chi^2$  minimization. This implies that the LTE assumption adopted by the above RD analysis is valid, and hence we obtain similar gas temperatures and CO column densities from the RD and LVG analyses. Similar  $\chi^2$  distribution patterns were found at other velocities. The reduced  $\chi^2$  ( $\chi_{\text{red}}^2$ ) of the best fitting results varies from 0.10 to 1.72 at different velocities. The representative uncertainty of each parameter is derived from the  $1\sigma$  confidence region in the 3D parameter space at the velocities where  $\chi_{\text{red}}^2 \sim 1$ : the relative uncertainty of the CO column density is  $\sim 10\%$ ; the temperature is found in the range of about 40 - 60 K; and the gas density is  $> 10^5 \text{ cm}^{-3}$  over the velocity range. The modeling results

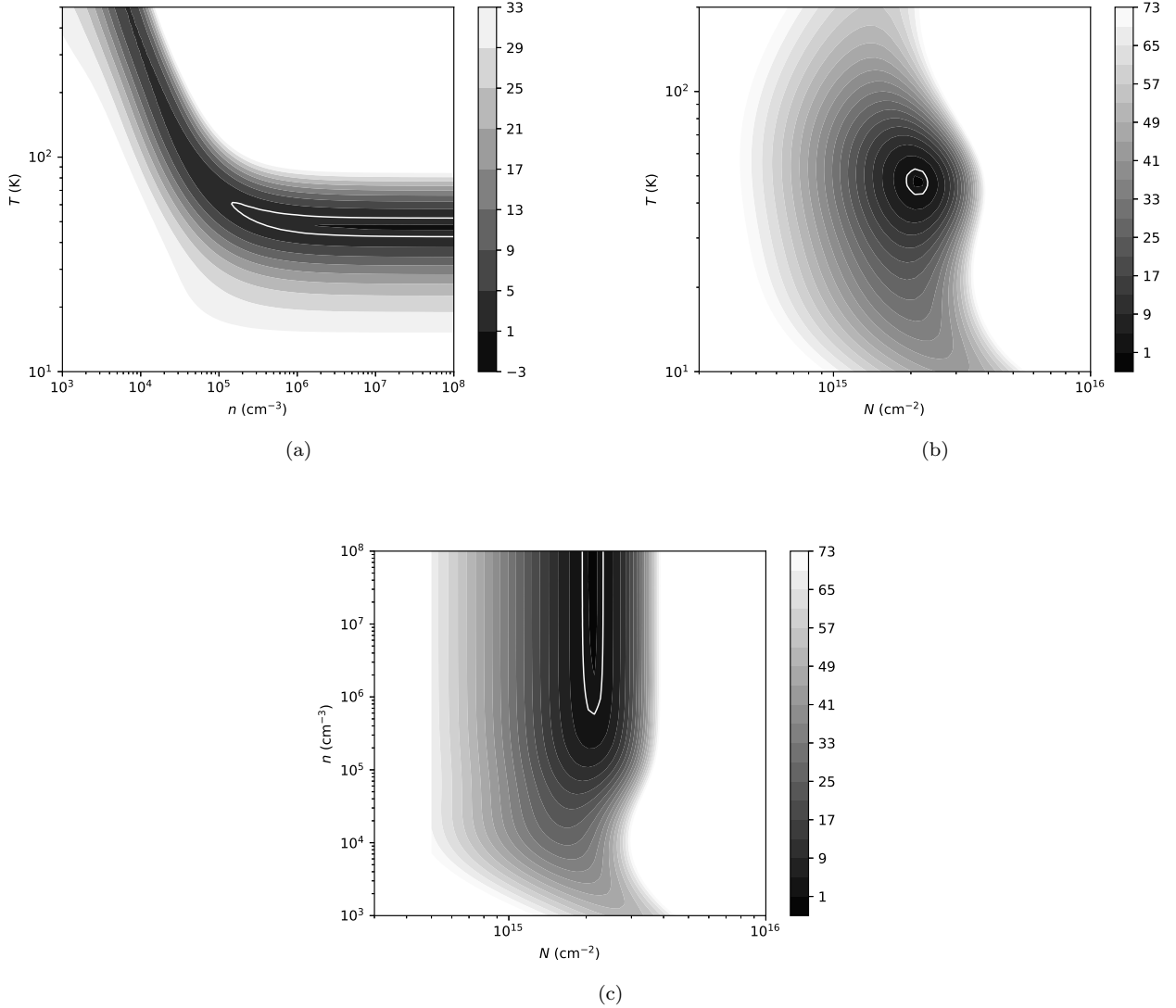


**Figure 4.** (a)-(c) The  $\chi^2$  distribution at 84 km s<sup>-1</sup> in the  $[T, n]$ ,  $[T, N]$  and  $[n, N]$  planes, with the third parameter fixed to the value of the best fitting result at this velocity. The lower limit of gas density is  $1.8 \times 10^5$  cm<sup>-3</sup>. The best-fit solution is obtained for  $T = 46.1$  K and  $N = 2.2 \times 10^{15}$  cm<sup>-2</sup>. The  $\chi^2_{\text{red}}$  of the best-fit solution is 1.00. The Solid white contours show the  $1\sigma$  confidence levels.

also predict that the four transitions are optically thin in the outflowing gas. Figure A1 shows the comparison of the observed CO intensities with the LVG modeling results in each velocity bin.

The variation of the physical conditions of the outflowing gas as a function of velocity is of great interests to our understanding of the driving mechanism of the outflow. With the RD and LVG analyses we have estimated the gas temperature, density and CO column density at different velocities. Figure 5 shows the temperature-velocity ( $T$ - $V$ ) and CO column density-velocity ( $N$ - $V$ ) relations. We performed RD and LVG analyses of the

CO lines in different positions, and obtained similar  $T$ - $V$  and  $N$ - $V$  relations.

## 4. DISCUSSION

### 4.1. Gas temperature

The morphology and kinematics of molecular outflows have been widely studied based on single spectral line observations. However, the physical conditions of the outflow gas are still not well constrained. In particular, how the physical conditions vary with the outflow velocity is poorly understood. van Kempen et al. (2009a) and Yıldız et al. (2012) performed LVG calculations on single-dish CO J = 3-2 and 6-5 lines, and suggested that



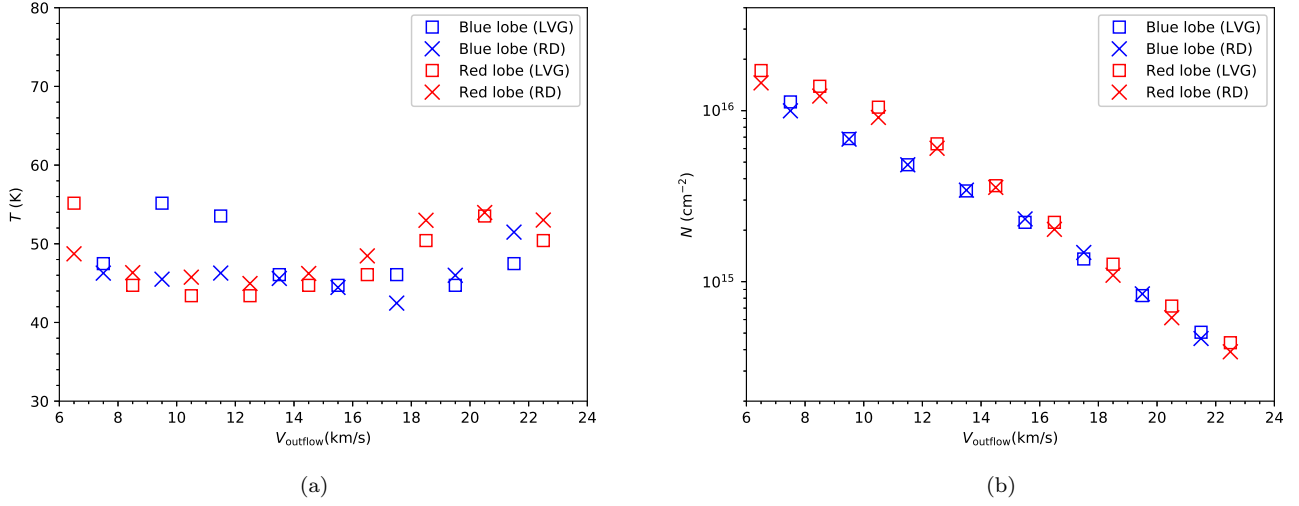


**Figure 5.**  $T$ - $V$  and  $N$ - $V$  diagrams of the G240 outflow, estimated from the rotation diagram analysis (blue “x” markers for the blue lobe and red “x” markers for the red lobe) and the LVG analysis (blue open squares for the blue lobe and red open squares for the red lobe).

there is little or no temperature change within outflow velocity ranges of  $< 10 - 15 \text{ km s}^{-1}$  in the outflow associated with low-mass protostars HH46 IRS1 and NGC 1333 IRAS 4A/4B. With interferometer CO  $J = 2-1$  and  $3-2$  observations, Su et al. (2012) performed an LVG analysis on the extremely high velocity outflow associated with the high-mass star-forming region G5.89-0.39, and found an increasing temperature with outflow velocity for outflow velocity  $< 160 \text{ km s}^{-1}$ . Based on the variation of the CO  $2-1/1-0$  line ratio and assuming LTE, Xie & Qiu (2018) found that the excitation temperature of the outflow of the massive star-forming region IRAS 22506+5944 increases from low ( $\sim 5 \text{ km s}^{-1}$ ) to moderate ( $\sim 8 - 12 \text{ km s}^{-1}$ ) velocities, and then decrease at higher velocities ( $< 30 \text{ km s}^{-1}$ ). In these works, assumptions about other outflow parameters (e.g. gas density, canonical CO fractional abundance and velocity gradient) or the equilibrium state (e.g. LTE) were made to infer the  $T$ - $V$  relations from only two CO lines, while these assumptions might not be necessarily valid. Other than that, the last two works have only used low- $J$  CO lines with small energy ranges, which are not sufficient to trace the relatively warm and dense gas. To more precisely determine the outflow properties, multi-line CO studies with sophisticated radiative transfer methods (e.g. LVG analysis) are needed. Recently, Lefloch et al. (2015) performed a multi-transition CO analysis on the outflow cavity ( $< 40 \text{ km s}^{-1}$ ) of the intermediate-mass Class 0 protostar Cepheus E-mm and revealed two gas components: the low-excitation component traced by CO transitions of  $J_{\text{up}} \leq 9$  is isother-

mal, and an increasing temperature of velocity is found in the high-excitation gas component traced by high- $J$  CO transitions (with  $J_{\text{up}}$  up to 16). Our analysis reveals that the G240 outflow, which is representative of a well-defined bipolar wide-angle molecular outflow in a  $> 10^4 L_{\odot}$  star-forming region (Qiu et al. 2009), is approximately isothermal with a gas temperature of  $\sim 50 \text{ K}$  within a outflow velocity range of  $23 \text{ km s}^{-1}$ . This isothermal state is similar to the behavior of outflows (traced by CO transitions of  $J_{\text{up}} \leq 9$ ) associated with low-mass and intermediate-mass protostars (Yildiz et al. 2012; Lefloch et al. 2015), and the temperature of  $\sim 50 \text{ K}$  is slightly lower than temperature constraints for outflows of low-mass protostars (van Kempen et al. 2009a; Yildiz et al. 2012) and intermediate-mass protostars (van Kempen et al. 2016). The derived outflow temperature is warmer than the previously adopted  $\sim 30 \text{ K}$  (Qiu et al. 2009), which indicates that the physical parameters (mass, momentum, energy) of the G240 outflow calculated by Qiu et al. (2009) were underestimated by a factor of 1.32.

#### 4.2. Gas density and CO column density

Figure 5 shows that, from  $\sim \pm 7 \text{ km s}^{-1}$  to  $\sim \pm 22 \text{ km s}^{-1}$  with respect to the cloud velocity, the beam-averaged CO column density decreases by a factor of 50. In the optically thin case, the CO column density  $N$  is related to the gas density  $n$  through the expression:

$$N = n \times \Delta V \times \frac{1}{dv/dr} \times X_{\text{CO}} \times f_{\text{b}}, \quad (2)$$

where  $f_b$  is the beam filling factor,  $X_{\text{CO}}$  the  $[\text{CO}]/[\text{H}_2]$  abundance ratio,  $\Delta V$  the velocity interval and  $dv/dr$  is the velocity gradient. The CO column density is degenerate with the beam filling factor, the velocity gradient and the abundance ratio. Assuming a constant CO abundance ratio, which is adopted by most previous works, the decreasing beam-averaged CO column density indicate a decline of beam-averaged gas column density with velocity. Since the beam filling factor only decreases by a factor of  $\sim 2.5$  within the outflow velocity range (derived from source sizes of  $\sim 20''$  to  $\sim 10''$ , see Figure 3 of Qiu et al. (2009)), it plays a minor role in the above relation. If the velocity gradient do not vary much, the variation of the beam-averaged CO column density and the beam filling factor indicates that the gas density decreases with velocity, and that the gas density is  $> 10^6 \text{ cm}^{-3}$  at the lowest outflow velocity. This gas density limit is comparable to the density of the low excitation component in the outflow cavity associated with Cepheus E-mm (Several times of  $10^5 \text{ cm}^{-3}$ : Lefloch et al. 2015).

#### 4.3. The origin of the G240 outflow

In a simple wide-angle wind-driven model, the gas temperature of the outflow is relatively constant, and the outflow density decreases with velocity and distance from the driving source (Shu et al. 1991; Arce et al. 2007). In contrast, the jet-driven bow shock model predicts that the gas temperature increases with outflow velocity. Our analysis results agree with the wind-driven model. Qiu et al. (2009) found that the kinematic structure and morphology of the G240 outflow can also be qualitatively interpreted by the wide-angle wind-driven model. Thus, we suggest that the G240 outflow is

mainly driven/entrained by a wide-angle wind, which itself may resemble the accretion-driven wide-angle winds (X-wind or disk winds: Shang et al. 2006; Pudritz et al. 2006) associated with low-mass YSOs, and we further suggest that disk-mediated accretion may exist in the formation of high-mass stars up to late-O types. It should be noted that most existing outflow models can only explain typical parameters of outflows driven by low-mass YSOs, and high-mass outflow models are necessary to quantitatively explain the physical conditions of outflows associated with high-mass YSOs. Statistical analyses of high-mass outflows are also essential for us to better understand the driven mechanism of massive outflows and the forming process of high-mass stars.

#### 5. SUMMARY

Using the APEX CO 3-2, 6-5 and 7-6 observations and the complementary CO 2-1 data, we have presented the first CO multi-transition study toward the molecular outflow of the high-mass star-forming region G240. The parsec-sized, bipolar, and high velocity outflow is clearly revealed by the CO 3-2, 6-5 and 7-6 emissions. For both lobes, the outflow is approximately isothermal with a temperature of  $\sim 50 \text{ K}$ . The outflowing gas is thermalized with a  $\text{H}_2$  density higher than  $n \sim 10^5 \text{ cm}^{-3}$ . The CO column density of the outflow decreases with gas velocity, which indicates that the gas density decreases with outflow velocity when the CO abundance and velocity gradient remain relatively constant. The isothermal state and the decreasing gas density indicate that the wind-driven/entrainment is the dominant driving mechanism of the G240 outflow. This finding further suggests that disk-accretion can be responsible for the formation of high-mass stars more massive than early B-type stars.

#### REFERENCES

- Arce, H. G., Shepherd, D., Gueth, F., et al. 2007, *Protostars and Planets V*, 245
- Banerjee, R., & Pudritz, R. E. 2006, *ApJ*, 641, 949
- Beuther, H., Schilke, P., Sridharan, T. K., et al. 2002, *A&A*, 383, 892
- Beuther, H., Schilke, P., Gueth, F., et al. 2002, *A&A*, 387, 931
- Caswell, J. L. 1997, *MNRAS*, 289, 203
- Caswell, J. L. 2003, *MNRAS*, 341, 551
- Choi, Y. K., Hachisuka, K., Reid, M. J., et al. 2014, *ApJ*, 790, 99
- Frank, A., Ray, T. P., Cabrit, S., et al. 2014, *Protostars and Planets VI*, 451
- Goldsmith, P. F., & Langer, W. D. 1999, *ApJ*, 517, 209
- Heyminck, S., Kasemann, C., Güsten, R., de Lange, G., & Graf, U. U. 2006, *A&A*, 454, L21
- Hughes, V. A., & MacLeod, G. C. 1993, *AJ*, 105, 1495
- Kasemann, C., Güsten, R., Heyminck, S., et al. 2006, *Proc. SPIE*, 6275, 62750N
- Kumar, M. S. N., Fernandes, A. J. L., Hunter, T. R., Davis, C. J., & Kurtz, S. 2003, *A&A*, 412, 175
- Lee, C.-F., Mundy, L. G., Reipurth, B., Ostriker, E. C., & Stone, J. M. 2000, *ApJ*, 542, 925
- Lee, C.-F., Stone, J. M., Ostriker, E. C., & Mundy, L. G. 2001, *ApJ*, 557, 429
- Lee, C.-F., Mundy, L. G., Stone, J. M., & Ostriker, E. C. 2002, *ApJ*, 576, 294

- Lefloch, B., Gusdorf, A., Codella, C., et al. 2015, *A&A*, 581, A4
- Li, G.-X., Qiu, K., Wyrowski, F., & Menten, K. 2013, *A&A*, 559, A23
- Machida, M. N., Inutsuka, S.-i., & Matsumoto, T. 2008, *ApJ*, 676, 1088-1108
- MacLeod, G. C., Scalise, E., Jr., Saedt, S., Galt, J. A., & Gaylard, M. J. 1998, *AJ*, 116, 1897
- Masson, C. R., & Chernin, L. M. 1993, *ApJ*, 414, 230
- Maud, L. T., Moore, T. J. T., Lumsden, S. L., et al. 2015, *MNRAS*, 453, 645
- Migenes, V., Horiuchi, S., Slysh, V. I., et al. 1999, *ApJS*, 123, 487
- Pudritz, R. E., Rogers, C. S., & Ouyed, R. 2006, *MNRAS*, 365, 1131
- Pudritz, R. E., Ouyed, R., Fendt, C., & Brandenburg, A. 2007, *Protostars and Planets V*, 277
- Qiu, K., Zhang, Q., Wu, J., & Chen, H.-R. 2009, *ApJ*, 696, 66
- Qiu, K., Zhang, Q., Menten, K. M., et al. 2014, *ApJL*, 794, L18
- Raga, A., & Cabrit, S. 1993, *A&A*, 278, 267
- Ren, J. Z., Liu, T., Wu, Y., & Li, L. 2011, *MNRAS*, 415, L49
- Sakai, N., Nakanishi, H., Matsuo, M., et al. 2015, *PASJ*, 67, 69
- Shang, H., Allen, A., Li, Z.-Y., et al. 2006, *ApJ*, 649, 845
- Shepherd, D. S., Watson, A. M., Sargent, A. I., & Churchwell, E. 1998, *ApJ*, 507, 861
- Shu, F. H., Ruden, S. P., Lada, C. J., & Lizano, S. 1991, *ApJL*, 370, L31
- Shu, F. H., Najita, J. R., Shang, H., & Li, Z.-Y. 2000, *Protostars and Planets IV*, 789
- Su, Y.-N., Liu, S.-Y., Chen, H.-R., & Tang, Y.-W. 2012, *ApJL*, 744, L26
- Trinidad, M. A. 2011, *AJ*, 142, 147
- van der Tak, F. F. S., Black, J. H., Schöier, F. L., Jansen, D. J., & van Dishoeck, E. F. 2007, *A&A*, 468, 627
- van Kempen, T. A., van Dishoeck, E. F., Güsten, R., et al. 2009, *A&A*, 501, 633
- van Kempen, T. A., van Dishoeck, E. F., Güsten, R., et al. 2009, *A&A*, 507, 1425
- van Kempen, T. A., Hogerheijde, M. R., van Dishoeck, E. F., et al. 2016, *A&A*, 587, A17
- Wu, Y., Wei, Y., Zhao, M., et al. 2004, *A&A*, 426, 503
- Wu, Y., Zhang, Q., Chen, H., et al. 2005, *AJ*, 129, 330
- Xie, Z.-Q., & Qiu, K.-P. 2018, *Research in Astronomy and Astrophysics*, 18, 019
- Yıldız, U. A., Kristensen, L. E., van Dishoeck, E. F., et al. 2012, *A&A*, 542, A86
- Zhang, Q., Hunter, T. R., Brand, J., et al. 2001, *ApJL*, 552, L167



## APPENDIX

## A. SPECTRAL LINE FLUX DISTRIBUTIONS

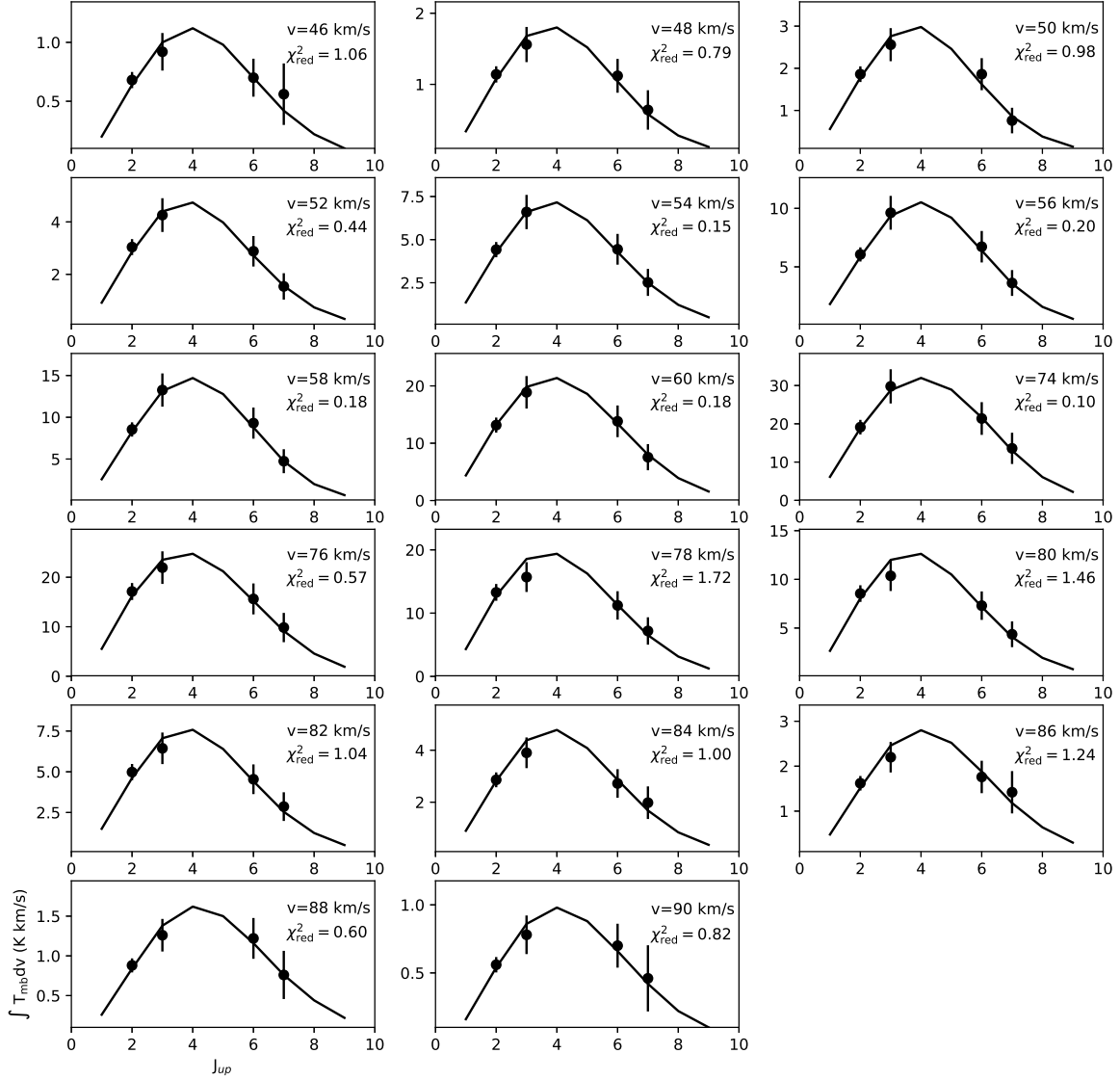


**Figure A1.** Observed line fluxes compared with the LVG computations in each 2 km/s bin. The black solid circles show the observed data with error bars. The black solid lines refer to the best fits. The  $\chi^2_{\text{red}}$  of the best fitting results and the outflow velocities are shown in each panel.